Ion loss on Mars caused by the Kelvin–Helmholtz instability

T. Penz [a,b,c,*], N. V. Erkaev [d], H. K. Biernat [c,a,b], H. Lammer [c], U. V. Amerstorfer [b,c], H. Gunell [e], E. Kallio [f], S. Barabash [e], S. Orsini [g], A. Milillo [g], and W. Baumjohann [c]

[a] *Institute for Theoretical Physics, University of Graz, Universitätsplatz 5, A–8010 Graz, Austria*

[b] *Institute for Geophysics, Astrophysics, and Meteorology, University of Graz, Universitätsplatz 5, A–8010 Graz, Austria*

[c] *Space Research Institute, Austrian Academy of Sciences, Schmiedlstr. 6, A–8042 Graz, Austria*

[d] *Institute for Computational Modelling, Russian Academy of Sciences, 660036 Krasnoyarsk–36, Russia*

[e] *Swedish Institute of Space Physics, P. O. Box 812, SE–98128 Kiruna, Sweden*

[f] *Finnish Meteorological Institute, Geophysical Research, P. O. Box 503, FIN–00101 Helsinki, Finland*

[g] *Instituto di Fisica dello Spazio Interplanetaro, Consiglio Nazionale delle Ricerche, Via Fosso del Cavaliere 100, I–00133 Roma, Italy*

Abstract

Mars Global Surveyor (MGS) detected cold electrons above the Martian ionopause, which can be interpreted as detached ionospheric plasma clouds. Similar observations by the Pioneer Venus Orbiter (PVO) electron temperature probe showed also extreme spatial irregularities of electrons in the form of plasma clouds on Venus, which were explained by the occurrence of the Kelvin-Helmholtz instability. Therefore, we suggest that the Kelvin-Helmholtz instability may also detach ionospheric plasma clouds on Mars. We investigate the instability growth rate at the Martian ionopause resulting from the flow of the solar wind for the case where the interplanetary magnetic field is oriented normal to the flow direction. Since the velocity shear near the subsolar point is very small, this area is stable with respect to the Kelvin-Helmholtz instability. We found that the highest flow velocities are reached at the equatorial flanks near the terminator plane, while the maximum plasma density in the terminator plane appears at the polar areas. By comparing the instability growth rate with the magnetic barrier formation time, we found that the instability can evolve into a non-linear stage at the whole terminator plane but preferably at the equatorial flanks. Escape rates of O^+ ions due to detached plasma clouds in the order of about 2×10^{23} to 3×10^{24} s^{-1} are found. Thus, atmospheric loss caused

by the Kelvin-Helmholtz instability should be comparable with other non-thermal loss processes. Further, we discuss our results in view of the expected observations of heavy ion loss rates by ASPERA-3 on board of Mars Express.

Key words: Mars, magnetohydrodynamics, instabilities, atmospheric loss

---

1 Introduction

Measurements of the Pioneer Venus Orbiter (PVO) spacecraft revealed a number of characteristic ionospheric structures that may be signatures of solar wind-ionosphere interaction processes (e.g., Brace et al., 1982; Russell et al., 1982). Among them are wavelike plasma irregularities, observed at the top of the dayside ionosphere and plasma clouds observed above the ionopause, primarily near the terminator and further downstream. The detailed analysis of several plasma clouds has shown that the plasma within the clouds themselves is ionosphere-like in electron temperature and density (Brace et al., 1982). When such plasma clouds were seen far above the ionosphere, they were clearly separated by an intervening region of magnetosheath plasma. This large separation in a direction perpendicular to the magnetosheath flow suggests that the ionospheric plasma in the clouds must have originated in the ionosphere upstream on the dayside, indicating that magnetohydrodynamic (MHD) instabilities may occur at the Venusian ionopause. Therefore, Elphic and Ershkovich (1984) analyzed the stability of the Venusian ionopause by using one-fluid MHD equations for a perfectly conducting, incompressible, inviscid fluid, and concluded that the Kelvin–Helmholtz instability is the dominant instability over most of the dayside ionopause.
The physical concept of the Kelvin-Helmholtz instability (Helmholtz, 1882; Lord Kelvin, 1910; Chandrasekhar, 1961) has been applied to space physics, first to describe the viscous interaction between the solar wind and an obstacle like the Earth's magnetosphere (Ong and Roderick, 1972; Nagano, 1978), or type 1 cometary tails (Ershkovich, 1980) and the Venusian solar wind–ionosphere interaction (Wolff et al., 1980). Additional analytical (Cloutier et al., 1983; Elphic and Ershkovich, 1984) and numerical analysis (Thomas and Winske, 1991) were applied to the Venusian ionopause.
Tanaka (1998) has modeled the solar wind interaction with the ionospheres of non-magnetized planets for different solar wind conditions by using a 3–D MHD model with a two-component plasma. Biernat et al. (1999, 2001) developed a MHD approach, which is partly analytical and partly numerical, to

* Corresponding author.
Email address: thomas.penz@stud.uni-graz.at (T. Penz).

investigate the 3-D flow around a planetary obstacle. Recently, Terada et al. (2002) used a global hybrid simulation to describe the Kelvin-Helmholtz instability at Venus. Further, Arshukova et al. (2004) showed that the Venusian ionopause can also be subject to the interchange instability.

The magnetometer carried aboard of Mars Global Surveyor (MGS) has clearly demonstrated that, like Venus, Mars does not have a significant, global, intrinsic magnetic field (Acuña et al., 1998; Connerney et al., 2001). Therefore, the global scale Martian solar wind interaction operates similar to that at the ionosphere/atmosphere of Venus (Shinagawa and Bougher, 1999; Liu et al., 1999, 2001; Ma et al., 2002). Acuña et al. (1998) reported the detection of cold electrons above the Martian ionopause, indicating the presence of detached plasma clouds in the magnetosheath of Mars.

Measurements by the ASPERA (Automatic Space Plasma Experiment with a Rotating Analyzer) instrument on board of Phobos 2 indicated a strong loss of plasma from the Martian topside ionosphere (Lundin et al., 1990). It was suggested that this ion loss results from ion pick up due to mass loading of the solar wind in the Martian boundary layer (Lichtenegger et al., 1995; Kallio et al., 1997; Lichtenegger and Dubinin, 1998; Lammer et al., 2003a). Lundin et al. (1990) reported the observation of a strong cold ion outflow and intense O^+ ion beams with energies up to several keV . Preliminary estimates of ionospheric outflow from Mars indicate that the planet may lose atomic oxygen at a rate of about 10^{25} s^{-1} during high solar activity.

Since the Martian upper atmosphere and ionosphere have a similar composition to Venus, the aim of this paper is to study under which solar wind and ionosphere conditions the Kelvin Helmholtz instability can occur at the Martian ionopause and how efficient its contribution to atmospheric escape of planetary ions due to detached plasma clouds is compared to other loss processes. We model the Kelvin-Helmholtz instability at the Martian ionopause for one-fluid, incompressible MHD equations. In the present study, we treat the solar wind flow past Mars in an MHD approximation which we have applied successfully to the case of the solar wind flow around Venus (Biernat et al., 1999; 2001). This approach is partly analytical and partly numerical.

By knowing the wavelength at the maximum instability growth rate, we can estimate the ion loss rate by scaling the observation of Brace et al. (1982) for Venus to the situation on Mars and compare the results with the atmospheric loss processes for atmospheric oxygen obtained by ion pick up, dissociative recombination, sputtering and surface weathering studied in detail by Lammer et al. (2003a).

2 Model calculation of the Kelvin-Helmholtz instability

In ideal MHD, the Kelvin-Helmholtz instability is analyzed by using the assumption of a zero Larmor radius of the particles. But in fact, this quantity is not negligible. Lerche (1966) showed that the ideal hydrodynamic analysis of the Kelvin-Helmholtz instability at the boundary layer leads to the conclusion that the waves with the shortest wavelength are the most unstable ones.
As a consequence, there would be no limit on the growth rate with decreasing wavelength. Therefore, the ideal MHD formulation of the Kelvin-Helmholtz instability is inapplicable to the stability problem at the interface of two interacting fluids with different shear velocities. The effect of finite ion Larmor radius was investigated by Nagano (1978, 1979) who demonstrated that the finite Larmor radius effect tends to stabilize short wavelength perturbations and helps to avoid the zero wavelength anomaly (Wolff et al., 1980). This stabilization can be seen in Figure 1.
Additionally, Wolff et al. (1980) and Elphic and Ershkovich (1984) included gravity, which acts to stabilize the interface against long wavelength perturbations (Figure 1). Terada et al. (2002) pointed out that this term works also effectively, when the density ratio across the discontinuity is large. According to Ong and Roderick (1972), the finite thickness of the boundary layer leads to the requirement that the wave number k for the maximum instability growth rate must satisfy the condition $k\,d/2 \approx 0.5$, where d is the thickness of the boundary layer.
In our model, we use a coordinate system, where X points from Mars to the Sun, Z is directed parallel to the IMF direction, and Y completes the right hand system. In such an IMF coordinate system, the components of the IMF are $(0, 0, |B_{IMF}|)$. We derive a dispersion relation for the case that the wave vector is parallel to the solar wind flow and perpendicular to the IMF direction ($\mathbf{k} \parallel \mathbf{u} \perp \mathbf{B}$). We use the dispersion relation appropriate for an incompressible plasma and an infinitely thin boundary layer including gravity and the finite Larmor radius effect (Wolff et al., 1980)

$$\omega = k\,\frac{\rho_1 u_1 + \rho_2 u_2}{\rho_1 + \rho_2} + k\,|k|\,\frac{\nu_2\rho_2 - \nu_1\rho_1}{\rho_1 + \rho_2} \pm i\,\gamma\,, \tag{1}$$

with

$$\gamma = \left(k^2 \frac{\rho_1\rho_2(u_2 - u_1)^2}{(\rho_1 + \rho_2)^2} + 2\left|k^3\right| \frac{(\nu_1 + \nu_2)\rho_1\rho_2(u_2 - u_1)}{(\rho_1 + \rho_2)^2} - \right.$$
$$\left. -k^4 \left(\frac{\nu_2\rho_2 - \nu_1\rho_1}{\rho_1 + \rho_2} \right)^2 - |k|\,\frac{g(\rho_2 - \rho_1)}{\rho_1 + \rho_2} \right)^{1/2}, \tag{2}$$

where ω is the frequency, and γ is the growth rate. u and ρ denote the plasma velocity and the plasma density, subscripts 1 and 2 denote magnetosheath and ionospheric conditions, respectively, and g is the gravitational acceleration at the ionopause. In the magnetosheath, the viscous coefficient is given as

$$\nu_1 = \frac{m_i u_1^2}{4\, e\, B_1}, \tag{3}$$

where m_i is the ion mass, e is the elementary charge and B is the magnetic field strength in the magnetosheath. Since $B \approx 0$ in the ionosphere, the viscous coefficient can be written as $\nu_2 = u_2\, l$, where l denotes the mean free path of the particles (Terada et al., 2002). If we assume that the IMF is not located purely in the Z direction, the surface is stabilized, since there exists a magnetic tension ($\sim (\mathbf{k}\cdot\mathbf{B})^2$), which impedes the Kelvin–Helmholtz instability (Elphic and Ershkovich, 1984).
Because the detachment of plasma clouds is a nonlinear process, it is a requirement that the characteristic timescales in the system are below the instability growth rate. If this is the case, the instability can evolve into a nonlinear stage, giving rise to the development of ionospheric plasma clouds. A characteristic time scale is the magnetic barrier formation time T_m (Arshukova et al., 2004), which can be estimated as the time of the transport of a frozen-in magnetic field line from the bow shock to the stagnation point

$$T_m = -\int_{1+\delta_p}^{x_s} \frac{1}{u_x}\, dx\,. \tag{4}$$

In this equation, the lower integration boundary is not exactly taken at the stagnation point, which has the distance 1 in normalized units (see Figure 2), in order to avoid a singularity in (7). Therefore, the lower integration boundary is shifted by the quantity δ_p, which is a small length scale, where the frozen-in condition is not valid, because of kinetic plasma effects (Arshukova et al., 2004). We consider this distance δ_p to be equal to the proton plasma scale, which is given as

$$\delta_p = \frac{c}{\omega_{pi}} \approx 100 \text{ km}\,, \tag{5}$$

where ω_{pi} is the proton gyro frequency. The upper integration boundary is the distance of the bow shock in normalized units $x_s = 1 + \Delta_s$, where Δ_s is the magnetosheath thickness (Figure 2). Taking a simple linear approximation for the velocity u_x along the stagnation stream line

$$u_x = -\frac{u_s(x-1)}{\Delta_s}\,, \tag{6}$$

we find the magnetic formation time as

$$T_m = \frac{\Delta_s}{u_s} \ln \frac{\Delta_s}{\delta_p} \,, \tag{7}$$

where u_s is the velocity just downstream of the shock. For applying the Kelvin-Helmholtz instability to Mars, it is necessary to know all the quantities mentioned above.

3 Occurrence of the Kelvin-Helmholtz instability in the Martian plasma environment

3.1 Plasma velocity and density conditions at the Martian magnetosheath

Even though a planet is unmagnetized, the flow of the solar wind is strongly affected by the interplanetary magnetic field (IMF). This interaction is studied by using a number of MHD approaches, used in a terrestrial context as well as for other planetary environments (e.g., Zwan and Wolf, 1976; Biernat et al., 1999). Studying the terrestrial magnetosheath, Zwan and Wolf (1976), Erkaev (1988), and others, predicted the presence of a region adjacent to the sunward side of the magnetopause where the influence of the magnetic field is very strong. In this so–called "magnetic barrier", the magnetic field increases, while remaining finite, and simultaneously the plasma density decreases there, thus this region is also named "plasma depletion layer". As a consequence, the plasma beta is below unity in this region.
Considering a steady-state situation, we model the plasma in a planetary magnetosheath as a nondissipative fluid which obeys the standard ideal MHD equations (in cgs units) (e.g., Weitzner, 1983) extended for mass loading processes

$$\begin{aligned} \nabla \cdot \left[\rho \mathbf{u}\mathbf{u} + \Pi \mathbf{I} - \frac{1}{4\pi} \mathbf{B}\mathbf{B} \right] &= 0 \,, \\ \nabla \cdot (\rho \mathbf{u}) &= N_0 m_0 s \,, \\ \nabla \cdot \mathbf{B} &= 0 \,, \\ \nabla \times (\mathbf{u} \times \mathbf{B}) &= 0 \,, \\ \nabla \cdot \left\{ \left[\frac{1}{2} \rho u^2 + \frac{\kappa}{\kappa - 1} p \right] \mathbf{u} + \frac{1}{4\pi} \mathbf{B} \times (\mathbf{u} \times \mathbf{B}) \right\} &= 0 \,. \end{aligned} \tag{8}$$

In (8), Π is the sum of the gas and magnetic pressures, $\Pi = p + B^2/8\pi$, while quantity ρ is the mass density. $\mathbf{B}$ and $\mathbf{u}$ are the magnetic field and plasma flow velocity, respectively. The parameter κ denotes the ratio of specific

heats ($\kappa = 5/3$), and $\mathbf{I}$ is the unit dyadic. In descending order, we have the momentum and mass conservation equations, the condition that the magnetic field is divergence–free, the induction equation of the magnetic field for an infinitely conducting fluid, and the energy conservation equation. N_0 and m_0 are the density and mass of neutral particles, respectively, while s is the ion production rate.
An important feature of the problem is that the solar wind flow upstream of the planetary bow shock is generally supersonic and superalfvénic, so that

$$p_\infty << \rho_\infty u_\infty^2 \,, \qquad \text{and} \qquad B_\infty^2 << 4\pi\rho_\infty u_\infty^2. \tag{9}$$

A consequence of these conditions is the existence of a detached shock separating the upstream interplanetary medium (denoted by ∞, and assumed uniform) from the magnetosheath. Across the shock the "Rankine–Hugoniot" jump relations must be satisfied (Biernat et al., 1999).
There are corresponding boundary conditions at the ionopause. We model this boundary as a tangential discontinuity satisfying

$$u_n = 0 \,, \qquad \text{and} \qquad B_n = 0. \tag{10}$$

We work with the following dimensionless variables

$$\begin{aligned} \mathbf{R}' &= \frac{\mathbf{R}}{R_0} \,, \\ p' &= \frac{p}{\rho_\infty u_\infty^2} \,, \\ \mathbf{B}' &= \frac{\mathbf{B}}{B_\infty} \,, \\ \mathbf{u}' &= \frac{\mathbf{u}}{u_\infty} \,, \end{aligned} \tag{11}$$

where $\mathbf{R}$ is the position vector (x, y, z), and R_0 is the curvature radius of the ionopause at the subsolar point. Further, we introduce a parameter ε, depending on the upstream quantities as

$$\varepsilon = \frac{B_\infty^2}{4\pi\rho_\infty u_\infty^2}. \tag{12}$$

This parameter is the inverse square of the Alfvén Mach number $M_{A\infty}$. Using the dimensionless set of variables, we transform the initial system of MHD equations (8) to the following set of equations:

$$\rho(\mathbf{u}\cdot\nabla)\mathbf{u} + \nabla\Pi = \varepsilon(\mathbf{B}\cdot\nabla)\mathbf{B} - q(\mathbf{R})\mathbf{u} \,,$$

$$
\begin{aligned}
\nabla \cdot (\rho \mathbf{u}) &= q(\mathbf{R}) \,, \\
\nabla \cdot \mathbf{B} &= 0 \,, \\
\nabla \times (\mathbf{u} \times \mathbf{B}) &= 0 \,, \\
\nabla \cdot \left\{ \left[\frac{1}{2} \rho u^2 + \frac{\kappa}{\kappa - 1} p \right] \mathbf{u} + \varepsilon \mathbf{B} \times (\mathbf{u} \times \mathbf{B}) \right\} &= 0 \,,
\end{aligned} \tag{13}
$$

with

$$\Pi = p + \varepsilon \, B^2/2.$$

Here $q(\mathbf{R})$ is a normalized ion source function,

$$q(\mathbf{R}) = q_0 exp(\frac{R_0 - R}{H_0}),$$

with

$$q_0 = N_0 m_0 s R_0/(\rho_\infty u_\infty),$$

and H_0 is the scale height of O. To estimate the mass loading parameter q_0 for Mars, we use an ion production term of $S = N_0 \, s = 5.85 \times 10^{-3}$ cm^{-3}s^{-1} (Lichtenegger et al., 2002). By using $R_0 = 3693$ km we achieve a typical value for the mass loading parameter of $q_0 \sim 0.5$.
We use the model shape of the ionopause which is a composite surface made up of a hemispherical surface (of radius R_0) on the sunward side smoothly attached to a surface of revolution on the nightside, given by

$$x = \begin{cases} 1.4 - 1.3 r^4, \; r \geq 0.98 \\ \sqrt{1 - r^2}, \quad r \leq 0.98 \,, \end{cases} \tag{14}$$

where $r = \sqrt{y^2 + z^2}$. Our ionopause flares out slightly on the nightside by an amount which decreases as we go further tailwards.
We integrate the MHD equations after bringing them to a special form, called "string equations" (see details in Biernat et al., 1999). The numerical scheme is based on the Lax-Wendroff method. We use a simplifying assumption concerning the behavior of the total pressure Π. In our method, its variation along the ionopause surface obeys the well–known Newtonian formula. (For the general applicability of the latter in the context of flow around planets, see the review by Petrinec and Russell (1997).) For the total pressure variations along the normal to the obstacle we use the quadratic approximation

$$\Pi = \Pi_m (1 - \frac{\mu^2}{\delta^2}) + \Pi_s \frac{\mu^2}{\delta^2}, \tag{15}$$

where μ is the distance from the ionopause along any given normal, and Π_m and Π_s are the values of the total pressures at the ionopause, and just downstream of the bow shock (with $\Pi_m > \Pi_s$), respectively, and δ is the distance from the ionopause to the bow shock along the normal. Quantity Π_s satisfies the jump conditions at the bow shock. For the variation of Π_m along the ionopause, we have

$$\Pi_m = (\Pi_0 - \Pi_\infty)\cos^2\theta + \Pi_\infty. \tag{16}$$

In this expression, Π_0 is the total pressure on the ionopause at the stagnation point of the flow, and θ is the angle between the radius vector to a given point on the obstacle and the stagnation streamline. However, the solution is not very sensitive to the precise variation of the total pressure as this quantity is the one which varies least in the (computed) magnetosheath and depletion layer.

In Figure 3, from top to bottom, the first two panels show variations of the mass density and the total velocity along different stream lines (1-9) at the ionospheric boundary. The corresponding stream lines are shown at the bottom panel. Each stream line starts from the stagnation line and goes along the ionopause. The stream line number 9 corresponds to the ionopause in the XY–plane for $Z = 0$. The dashed line shows the shape of the obstacle in the XZ–plane at $Y = 0$. One can see in Figure 3, that the highest plasma flow velocities appear at the flanks near the equatorial plane, where the velocity reaches about 0.9 u_∞. This results from the fact that magnetic forces destroy the axial symmetry of the plasma flow around the ionosphere. The plasma flow is accelerated at the flanks in direction perpendicular to the magnetic field lines. This acceleration is caused by strong magnetic field tension in the magnetic barrier.

Near the terminator, the velocity is only about 0.3 u_∞ and near the subsolar point, the velocity tends to zero, indicating that this region is stable against the Kelvin-Helmholtz instability, as also pointed out by Elphic and Ershkovich (1984) and Luhmann (1990). The plasma density reaches values of about 3 n_∞ near the subsolar point, while it decreases to n_∞ at the terminator and at the flanks in the equatorial plane.

3.2 The situation near the subsolar point

Our model gives flow velocities in the magnetosheath of about $u_1 = 0.1\,u_\infty$, and plasma densities of $n_1 = 3.5\,n_\infty$ (Figure 3). Taking a magnetic field strength of $B_1 = 20$ nT (Acuña et al., 1998) in the magnetosheath close to the subsolar point, the viscous coefficient is $\nu_1 = 200$ km^2/s, by assuming that the plasma in the magnetosheath mainly consist of protons.

The altitude of the subsolar ionopause was observed at about 300 km during

the entry of the Viking 2 probe (Hanson et al., 1977). Also Mars Global Surveyor measurements indicate an ionopause altitude of about 350 km (Mitchell et al., 2001), which is consistent with calculations by Ma et al. (2002). At an altitude of about 300 km, the gravitational acceleration is $g \approx 3.15$ km/s^2 and the ion temperature is about 1700 K (Hanson et al., 1977; Barth et al., 1992), which results in a viscous coefficient of $\nu_2 \approx 1000$ km^2/s.
Measurements of both Viking landers established that the principal ion in the Martian ionosphere does not correspond to the main ionizable neutral constituent CO_2, but is O_2^+, in a manner analogous to the case of the Venusian ionosphere (Hanson et al., 1977). In addition, the O^+ concentration becomes comparable to that of O_2^+ at altitudes above 280 km, and also H^+ has a certain contribution to the ion density at these altitudes. According to Barth et al. (1992), we use an O_2^+ density of about 7×10^2 cm^{-3}, an O^+ density of about 2×10^2 cm^{-3}, and a H^+ density of about 50 cm^{-3} at the subsolar ionopause altitude.
Therefore, we get a mass density $\rho_2 = (7\times10^2\times32+2\times10^2\times16+50)$ cm^{-3} $\times\, m_p$ $\approx 2.5\times10^4$ cm^{-3} $\times\, m_p$ in the ionosphere. By applying our model to this case, we obtain instability growth rates $\gamma < 10^{-5}$ s^{-1}, which can be compared with the inverse of the magnetic barrier formation time. The distance of the bow shock is $\Delta_s \approx 1.5\, R_M$ (Luhmann et al., 1992) and $u_s = (\rho_\infty/\rho_s)u_\infty \approx u_\infty/3$. Using a solar wind velocity of 250 km/s, the magnetic barrier formation time is $T_M = 240$ s, and 150 s for a solar wind velocity of 400 km/s. It follows that the characteristic frequency for 250 km/s is 4×10^{-3} s^{-1} and for 400 km/s it is 7×10^{-3} s^{-1}.
Therefore, it seems reasonable that the subsolar ionopause of Mars is stable with respect to the Kelvin-Helmholtz instability. If we consider model calculations of Shinagawa and Cravens (1989), which included ion loss due to the divergence of the horizontal velocity field, the particle density at 300 km is $\rho_2 = (2 \times 10^2 \times 16 + 40 \times 32 + 40 \times 44)$ cm^{-3} $\times\, m_p \approx 6 \times 10^3$ cm^{-3} $\times\, m_p$, where the last term corresponds to CO_2^+ ions. We find that this also results in growth rates many orders of magnitude below the magnetic barrier formation time so that the ionopause is stable against the Kelvin-Helmholtz instability.

3.3 The situation near the polar terminator

One can see from Figure 3 that the flow velocity in the magnetosheath near the terminator is about $u_1 \approx 0.3\, u_\infty$, while the density is $n_1 \approx n_\infty$. Measurements of Mars Global Surveyor (Acuña et al., 1998) and radio occultation experiments indicate that the distance of the ionopause for high solar zenith angle may lie between 300 and 500 km, while certain model calculations (Kallio, 1996; Ma et al., 2002) use altitudes of at least 1000 km.
Since the measurements of the quantities needed to calculate the instability growth rate are very poor, we want to consider different cases, which may

appear on Mars. We model the situation for a medium solar wind velocity of $u_\infty = 400$ km/s (Case 1), and for a low solar wind velocity of $u_\infty = 250$ km/s (Case 2). Additionally, we consider the case of a low–altitude ionopause at 400 km altitude, and the case of an ionopause altitude of 1000 km in the terminator plane.

For the first case with medium–speed solar wind conditions, the magnetosheath flow velocity is $u_1 = 120$ km/s. Considering a low–altitude ionopause, we use the ionospheric parameters of Shinagawa and Cravens (1989), where they assumed an induced magnetic field of 60 nT, resulting in an O^+ density of about 5×10^2 cm^{-3} and a H^+ density of about 10^2 cm^{-3} at 400 km altitude. This gives a mass density $\rho_2 = (5 \times 10^2 \times 16 + 10^2)$ cm^{-3} $\times\ m_p \approx 8 \times 10^3$ cm^{-3} $\times\ m_p$. Using an ion temperature of 2000 K (Barth et al., 1992), the viscous coefficient in the ionosphere is $\nu_2 = 260$ km^{2}s^{-1}, while the viscous coefficient in the magnetosheath is $\nu_1 = 630$ km^2/s. For this case, we achieve maximum growth rates of about $\gamma = 10^{-2}$ s^{-1} (Figure 4a) at a wavelength of 150 km. Because the characteristic frequency in this case is about 7×10^{-3} s^{-1}, the instability can occur for medium–speed solar wind condition.

For the case of a high–altitude ionopause at about 1000 km, we can assume much smaller ionospheric particle densities, e.g., $\rho_2 = 800$ cm^{-3} $\times\ m_p$, corresponding to an O^+ density of 50 cm^{-3}. For an induced magnetic field of 20 nT, the viscous coefficient in the magnetosheath is $\nu_1 \approx 730$ km^2/s. For the ionosphere, if we use an ion temperature of about 2400 K (Barth et al., 1992) and an ion velocity of 100 m/s (Shinagawa and Cravens, 1989), we get the viscous coefficient as $\nu_2 \approx 3800$ km^2/s. The maximum instability growth rates obtained in this case are about $\gamma = 10^{-2}$ s^{-1} (Figure 4b), which is again below the characteristic frequency. The corresponding wavelength is approximately 800 km.

Since there is a large uncertainty regarding the ionospheric particle density at a height of 1000 km, we want to study two additional cases, for an O^+ density of 100 cm^{-3} and of 20 cm^{-3}. For the first case, the growth rate and the wavelength are slightly smaller than for an O^+ density of 60 cm^{-3}. For the second case with a small particle density, the growth rate is below the characteristic frequency of 7×10^{-3} s^{-1}, but the result is also very sensitive with respect to the magnetosheath velocity, because if we assume a magnetosheath velocity $u_1 = 150$ km/s instead of 120 km/s, the growth rate is about 2×10^{-2} s^{-1}.

For low–speed solar wind conditions (Case 2) of $u_\infty = 250$ km/s, the magnetosheath velocity is $u_1 = 75$ km/s. For both, a high– and a low–altitude ionopause, the growth rates are about 10^{-3} s^{-1}, while the characteristic frequency is 4×10^{-3} s. Therefore, the Kelvin-Helmholtz instability will not occur at the polar terminator, if low–speed solar wind conditions are assumed.

3.4 The situation at the equatorial flanks near the terminator plane

We calculated a flow velocity of $u_1 \approx 0.9\, u_\infty$ in the region at the equatorial flanks near the terminator plane. The density in this region is close to the solar wind density. We consider again both cases mentioned in the previous section.
For a medium solar wind velocity of $u_\infty = 400$ km/s, the magnetosheath velocity is $u_1 = 360$ km/s. For an ionopause altitude of about 400 km and an ionosphere density of $\rho_2 = 8 \times 10^3$ cm^{-3} $\times$ m_p, the viscous coefficients are $\nu_1 = 5600$ km^2/s and $\nu_2 = 260$ km^2/s, respectively. The instability growth rate for this case is $\gamma = 7 \times 10^{-2}$ s^{-1}, corresponding to a wavelength of about 60 km (Figure 5a). For these small wavelengths, the finite boundary thickness must be taken into account. If we assume a so-called "thin ionopause" (Mahajan and Mayr, 1990), the ionopause thickness is about 20 km, which was also used by Shinagawa and Bougher (1999). In this case, the requirement that $k\, d/2 \approx 0.5$ must be fulfilled. To fulfil this condition, the ionopause thickness must be less than 10 km for the maximum growth rate, which is not realistic. But for a boundary thickness of 20 km, the growth rates are as large as $\gamma = 4$ x 10^{-2} s^{-1} (Figure 5a) and for 30 km, $\gamma = 3$ x 10^{-2} s^{-1} , which is also below the characteristic frequency of about 7×10^{-3} s^{-1}. For a high–altitude ionopause, the viscous coefficients are $\nu_1 = 16900$ km^2/s and $\nu_2 = 3800$ km^2/s. This leads to a maximum growth rate of $\gamma = 5$ x 10^{-2} s^{-1} at a wavelength of about 200 km (Figure 5b). The magnetic barrier formation time in this case is 150 s, and therefore the Kelvin–Helmholtz instability can evolve at the equatorial flanks.
For low–speed solar wind conditions the magnetosheath velocity is $u_1 = 225$ km/s. A low–altitude ionopause leads to viscous coefficients of $\nu_1 = 2200$ km^2/s and $\nu_2 = 260$ km^2/s, respectively. Therefore, a growth rate of $\gamma = 3$ x 10^{-2} s^{-1} at a wavelength of 100 km is achieved. A high–altitude ionopause leads to a growth rate of $\gamma = 2$ x 10^{-2} s^{-1}, but at large wavelengths of about 500 km. Since the characteristic frequency for low solar wind velocities is about 4×10^{-3} s^{-1}, the Kelvin–Helmholtz instability will also occur in this case.

3.5 Ion loss due to instability induced detached plasma clouds

Brace et al. (1982) estimated from the PVO observations that on average, about 12 ionospheric plasma clouds were present at any given time in the cloud zone at Venus. This estimation is based on the assumption that the probability of observing a cloud would be approximately the ratio of the cross sectional area of the cloud to the total area of the observable zone. This ratio is about 1/20, which means one plasma cloud in 20 should be detected. Thus, if only one cloud is in the observable zone, there is a 5 % chance of observing it on any downstream passage through the zone.

Instead, PVO observed clouds on 20 % of the orbits, a fact which suggests that an average of four plasma clouds were in the observable zone at any given time. Since, only about 1/3 of the zone was observed by PVO, Brace et al. (1982) assumed that there are an average of $n_c = 12$ clouds somewhere in the zone at any given time. If we scale the Venusian ionopause surface to the Martian geometry, we can expect that about 4 clouds may be present in the Martian magnetosheath at any time. Now we can assume that the time for the development of a plasma cloud lies in the range of the magnetic barrier formation time T_M, which is in the range of 120 to 240 s. Therefore, the ion escape rate f can be estimated as (Brace et al., 1982)

$$f \approx \frac{n_i n_c}{T_M}\,, \tag{17}$$

where n_i is the number of ions in one plasma cloud, and n_c is the cloud number. The number of ions in one plasma cloud can be estimated for an assumed cylindrical shape as the product of the plasma cloud volume and the ionospheric plasma density in the region, where the cloud detaches from the ionosphere. We assume that the cloud has a cylindrical configuration with a radius of half of the instability wavelength and a height of 1000 km (Brace et al., 1982).

Near the polar terminator, we found that the Kelvin–Helmholtz instability will occur only for medium–speed solar wind conditions. For a low–altitude ionopause, we take an ionospheric particle density of 8000 cm^{-3} and a wavelength of 150 km. Therefore, the ion escape rate can be determined as $f = 5.7 \times 10^{24}$ particles/s. This corresponds to a loss of about 3.5×10^{23} O^+/s and 3.5×10^{21} H^+/s. For a high–altitude ionopause, the ionosphere density is about 800 cm^{-3} and the wavelength is about 800 km. The ion escape rate for this case is $f = 1.6 \times 10^{25}$ particles/s, giving an O^+ loss of 10^{24} s^{-1}.

At the flanks, the Kelvin–Helmholtz instability occurs for medium– and low–speed solar wind conditions. For medium–speed solar wind conditions and a low–altitude ionopause, an escape rate of $f = 9.1 \times 10^{23}$ particles/s is found. This gives an O^+ loss of about 6×10^{22} s^{-1} and of about 6×10^{20} H^+/s. A high–altitude ionopause gives a slightly larger escape rate of $f = 10^{24}$ particles/s, which yields an O^+ escape of 6.5×10^{22} s^{-1}. For low–speed solar wind conditions, we found higher escape rates. For a low–altitude ionopause, we achieve an ion escape rate of 2.5×10^{24} particles/s, corresponding to a loss of 1.5×10^{23} O^+/s and 1.5×10^{21} H^+/s. A high–altitude ionopause leads to an escape rate of $f = 6.3 \times 10^{24}$ particles/s, giving an O^+ loss of 4×10^{23} s^{-1}. Since we have shown that the instability growth rates at the flanks are nearly one order–of–magnitude higher than near the polar terminator, it is reasonable to assume that most of the clouds will detach in this region, which was not studied by Brace et al. (1982). Therefore, we assume that the total number of clouds detaching from the ionopause can reach 30 clouds at any given time. This assumption gives escape rates for medium–speed solar wind

conditions of $f = 6.8 \times 10^{24}$ particles/s and $f = 7.5 \times 10^{24}$ particles/s for low and high ionopause altitudes, respectively. The corresponding O+ escape rates are 4.3×10^{23} s^{-1} and 4.7×10^{23} s^{-1}, while the H^+ escape rate is 4.3×10^{21} s^{-1} for a low–altitude ionopause. For low–speed solar wind conditions, we get escape rates of $f = 1.9 \times 10^{25}$ particles/s and $f = 4.7 \times 10^{25}$ particles/s, again for low and high ionopause altitudes. The O^+ escape achieved under these conditions is 1×10^{24} s^{-1} and 3×10^{24} s^{-1}, respectively, while the H^+ escape rate is 1.2×10^{22} s^{-1} for a low–altitude ionopause.
By comparing these loss rates of O^+ ions due to detached plasma clouds with loss rates of very low energetic O atoms from dissociative recombination of about 5.0×10^{24} s^{-1} (Lammer and Bauer, 1991; Fox, 1993; Luhmann, 1997, Kim et al., 1998), 3-D-sputter model results of O atoms of about 4.3×10^{23} s^{-1} (Leblanc and Johnson, 2002) and modeled ion pick up escape rates during medium–speed solar wind conditions of about 3×10^{24} s^{-1} (Lammer et al., 2003a), one can see that the Kelvin-Helmholtz instability may remove ions from Mars in comparable amounts (Table 1). The loss of H^+ ions can be neglected compared with other processes. One can see that at present the total average loss of oxygen from Mars is about 1.5×10^{25} s^{-1} and fails by far to balance the total thermal and nonthermal escape flux of hydrogen of about 1.8×10^{26} s^{-1}. Since hydrogen and oxygen lost to space are believed to have their origin from photo-dissociation of H_2O vapor in the Martian atmosphere, the difference between the oxygen and hydrogen loss to space, needed for the validation of a 2:1 ratio between H and O, can be explained by the incorporation into the Martian surface by chemical weathering processes (Lammer et al., 1996, 2003a, 2003b; Patel et al., 2003).

4 Conclusions

Our study concerning the occurrence of the Kelvin-Helmholtz instability at the Martian ionopause yields O^+ ion loss rates of about 2×10^{23} to 3×10^{24} s^{-1} depending mainly on the solar wind conditions, the ionopause altitude and the ionospheric plasma density. We suggest that the Kelvin-Helmholtz instability contributes efficiently to the erosion of ionospheric particles and may explain the difference between photo-chemical ionospheric equilibrium models (Kar et al., 1996) and observed ion density profiles on Mars. Further, this loss process may also be necessary to achieve observed ion density profiles in MHD models (Shinagawa and Cravens, 1989). On the other hand, we found several limitations, which restrict the occurrence of the Kelvin–Helmholtz instability. If the density ratio between the magnetosheath and the ionosphere is large, like it was on early Mars, the Kelvin–Helmholtz instability may not occur. For high viscous coefficients, the wavelengths are shifted to large values and the insta-

bility growth rates decrease. Such large viscous coefficients can be achieved in the ionosphere, if momentum transfer (Pérez–de–Tejada, 1998) accelerates the ions in the upper ionosphere to velocities of more than 5 km/s, but in this case, the ions may escape since their velocity is larger than the escape velocity on Mars. If the induced magnetic field at the ionopause is large, e.g., more than 40 nT, the viscous coefficients are smaller, which makes the occurrence of the Kelvin–Helmholtz instability more likely. Maybe, remnant, local magnetism (Ma et al., 2002) will support the development of plasma clouds at the Martian ionopause. Additionally, in our approach the bow shock and the ionopause are assumed to be axially symmetric, and therefore this model contains no asymmetries associated with finite gyroradius effects, especially of the O^+ ions. In future, we want to investigate in more detail the influence of the mass loading term on the evolution of the Kelvin–Helmholtz instability.
If plasma clouds, like those observed at Venus and predicted in our paper, are also present above the Martian ionopause they are likely to be measured by the ASPERA–3 instrument during ESA's Mars Express mission. The periapsis of Mars Express will be about 280 km, and during the mission the Martian plasma environment above the ionopause will be probed for the first time over a whole range of solar zenith angles. The ASPERA-3 instrument contains an electron spectrometer (ELS) that is capable of measuring electrons in the energy range 0.01-20 keV, and an ion mass analyzer (IMA) for measurements in the energy range between 0.01 to 40 keV/q of the main ion components H^+, H_2^+, He^+, O^+, and the group of ions with M/q between 20 and 80. However, the total ion outflow measurements on Mars by the ASPERA-3 instrument will reduce the uncertainties in the current estimations of atmospheric/water loss caused by solar wind plasma interactions with the ionospheric environment such as ionospheric clouds and momentum transfer effects.

Acknowledgements: The authors thank Richard P. Rijnbeek for very useful suggestions and comments. Part of this work was done while H. K. B. was on a research visit to the Institute of Computational Modelling of the Russian Academy of Sciences in Krasnoyarsk, Siberia, and to the Instituto di Fisica dello Spazio Interplanetario, Consiglio Nazionale delle Ricerche, in Roma, Italy. This work is supported by the Austrian "Fonds zur Förderung der wissenschaftlichen Forschung" under projects P13804–TPH and P17099–N08, by grants No 04–05–64088 and No 03-05-20014 from the Russian Foundation of Basic Research, by grants E02–8.0–22 and A03-2.13-469 from the Russian Ministry of Higher Education, and by projects No. I.2/04 and No. I.12/04 from the "Österreichischer Austauschdienst". Also acknowledged is support by the Austrian Academy of Sciences, "Verwaltungsstelle für Auslandsbeziehungen" and by the Russian Academy of Sciences. T. P. acknowledges support through a "Paul–Urban–Stipendium" from the Institute of Theoretical Physics of the University of Graz.

References

Acuña, M. H., et al., 1998. Magnetic field and plasma observations at Mars: Initial results of the Mars Global Surveyor mission, Science, 279, 1676–1680.

Arshukova, I. L., N. V. Erkaev, H. K. Biernat, and D. F. Vogl, 2004. Interchange instability of the Venusian ionopause, Adv. Space Res., 33, 182–186.

Barth, C. A., A. I. F. Stewart, S. W. Bougher, D. M. Hunten, S. J. Bauer, and A. F. Nagy, 1992. Aeronomy of the current Martian atmosphere, in Mars, H. H. Kieffer, B. M. Jakosky, C. W. Snyder, and M. S. Matthews (Eds.), University of Arizona Press, Tucson, 1054–1089.

Biernat, H. K., N. V. Erkaev, and C. J. Farrugia, 1999. Aspects of MHD flow about Venus, J. Geophys. Res., 104, 12617–12626.

Biernat, H. K., N. V. Erkaev, and C. J. Farrugia, 2001. MHD effects in the Venus magnetosheath including mass loading, Adv. Space Res., 28, 833–839.

Brace, L. H., R. F. Theis, and W. R. Hoegy, 1982. Plasma clouds above the ionopause of Venus and their implications, Planet. Space Sci., 30, 29–37.

Chandrasekhar, S., 1961. Hydrodynamic and hydromagnetic stability, Oxford Univ. Press, New York.

Cloutier, P. A., T. F. Tascione, R. E. Daniell Jr., H. A. Taylor, and R. S. Wolff, 1983. Physics of the interaction of the solar wind with the ionosphere of Venus: Flow/field models, in Venus, D. M. Hunten (Ed.), Univ. of Arizona Press, Tucson, 941–979.

Connerney, J. E. P., M. H. Acuña, P. J. Wasilewski, G. Kletetschka, N. F. Ness, H. Rème, R. P. Lin, and D. L. Mitchell, 2001. The global magnetic field of Mars and implications for crustal evolution, Geophys. Res. Lett., 28, 4015–4018.

Elphic, R. C., and A. I. Ershkovich, 1984. On the stability of the ionopause of Venus, J. Geophys. Res., 89, 997–1002.

Erkaev, N. V., 1988. Results of the investigation of MHD flow around the magnetosphere (review), Geomag. Aeron., 28, 455–461.

Ershkovich, A. I., Kelvin–Helmholtz instability in type–1 comet tails and associated phenomena, 1980. Space Sci. Rev., 25, 3–34.

Fox, J. L., 1993. On the escape of oxygen and hydrogen from Mars, Geophys. Res. Lett., 20, 1847–1850.

Hanson, W. B., S. Sanatani, and D. R. Zuccaro, 1977. The Martian ionosphere as observed by the Viking retarding potential analyzer, J. Geophys. Res., 82, 4351–4363.

Helmholtz, H., 1882. Über diskontinuierliche Fluessigkeitsbewegungen, in Wissenschaftliche Abhandlungen, J. A. Barth, Leipzig.

Kallio, E., 1996. An empirical model of the solar wind flow around Mars, J. Geophys. Res., 101, 11133–11147.

Kallio, E., J. G. Luhmann, and S. Barabash 1997. Charge exchange near Mars: The solar wind absorption and energetic neutral atom production, J. Geophys. Res., 102, 22183–22197.

Kar, J., K. K. Mahajan, and R. Kohli 1996. On the outflow of O_2^+ ions at

Mars, J. Geophys. Res., 101, 12747–12752.
Kim, J., A. F. Nagy, J. L. Fox, and T. Cravens, 1998. Solar cycle variability of hot oxygen atoms at Mars, J. Geophys. Res., 103, 29339–29342.
Lammer, H., and S. J. Bauer, 1991. Nonthermal atmospheric escape from Mars and Titan, J. Geophys. Res., 96, 1819–1825.
Lammmer, H., W. Stumptner, and S. J. Bauer, 1996. Loss of H and O from Mars: implications for the planetary water inventory, Geophys. Res. Lett., 23, 3353–3356.
Lammer, H., H. I. M. Lichtenegger, C. Kolb, I. Ribas, E. F. Guinan, R. Abart, and S. J. Bauer, 2003a. Loss of water from Mars: Implications for the oxidation of the soil, Icarus, 106, 9–25.
Lammer, H., C. Kolb, T. Penz, U. V. Amerstorfer, H. K. Biernat, and B. Bodiselitsch, 2003b. Estimation of the past and present Martian water ice reservoirs by isotopic constraints on exchange between the atmosphere and the surface, Int. J. Astrobiology, 2 (3), 195–202.
Leblanc, F., and R. E. Johnson, 2002. Role of molecular species in pick up ion sputtering of the Martian atmosphere, J. Geophys. Res., 107, E2, (5), 1–6.
Lerche, I., 1966. Validity of the hydrodynamic approach in discussing instability of the magnetospheric boundary, J. Geophys. Res., 71, 2365–2371.
Lichtenegger, H. I. M., K. Schwingenschuh, E. M. Dubinin, and R. Lundin, 1995. Particle simulation in the Martian magnetotail, J. Geophys. Res., 100, 21659–21667.
Lichtenegger, H. I. M., and E. M. Dubinin, 1998. Model calculations of the planetary ion distribution in the Martian tail, Earth Planets Space, 50, 445–452.
Lichtenegger, H. I. M., H. Lammer and W. Stumptner, 2002. Energetic neutral atoms at Mars: III. Flux and energy distribution of planetary energetic H atoms, J. Geophys. Res., 107(A10), 1279, doi:10.1029/2001JA000322.
Liu, Y., A. F. Nagy, C. P. T. Groth, D. L. DeZeeuw, T. I. Gombosi, and K. G. Powell, 1999. Three–dimensional multifluid MHD studies of the solar wind interaction with Mars, Geophys. Res. Lett., 26, 2689–2692.
Liu, Y., A. F. Nagy, T. I. Gombosi, D. L. DeZeeuw, and K. G. Powell, 2001. The solar wind interaction with Mars: Results of three–dimensional three–species MHD studies, Adv. Space Res., 27, 1837.
Lord Kelvin, 1910. Hydrokinetic solutions and observations, in Mathematical and physical papers IV, Hydrodynamics and general dynamics, Cambridge.
Luhmann, J. G., 1990. Wave analysis of Venus ionospheric flux ropes, in Physics of magnetic flux ropes, C. T. Russell, E. R. Priest, and L. C. Lee (Eds.), Geophysical Monograph 58, American Geophysical Union, Washington, 425–432.
Luhmann, J. G., C. T. Russell, L. H. Brace, and O. L. Vaisberg, 1992. The intrinsic magnetic field and solar–wind interaction of Mars, in Mars, H. H. Kieffer, B. M. Jakosky, C. W. Snyder, and M. S. Matthews (Eds.), University of Arizona Press, Tucson, 1090–1134.
Luhmann, J. G., 1997. Correction to "The ancient oxygen exosphere of Mars:

implications for atmospheric evolution", J. Geophys. Res., 102, 1637.
Lundin, R., A. Zakharov, R. Pellinen, S. W. Barabash, H. Borg, E. M. Dubinin, B. Hultquist, H. Koskinen, I. Liede, and N. Pissarenko, 1990. ASPERA/Phobos measurements of the ion outflow from the Martian ionosphere, Geophys. Res. Lett., 17, 873–876.
Ma, Y., A. F. Nagy, K. C. Hansen, D. L. DeZeeuw, T. I. Gombosi, and K. G. Powell, 2002. Three–dimensional multispecies MHD studies of the solar wind interaction with Mars in the presence of crustal fields, J. Geophys. Res., 107(A10), 1282–1288, doi:10.1029/2002JA009293.
Mahajan, K. K., and H. G. Mayr, 1990. Mars ionopause during solar minimum: A lesson from Venus, J. Geophys. Res., 95, 8265–8269.
Mitchell, D. L., R. P. Lin, C. Mazelle, H. Reme, P. A. Cloutier, J. E. P. Connerney, M. H. Acuna, and N. F. Ness, 2001. Probing Mars' crustal magnetic field and ionosphere with the MGS Electron Reflectometer, J. Geophys. Res., 106, 23419–23427.
Nagano, H., 1978. Effect of finite ion Larmor radius on the Kelvin–Helmholtz instability, J. Plasma Phys., 20, 149–160.
Nagano, H., 1979. Effect of finite ion Larmor radius on the Kelvin–Helmholtz instability of the magnetopause, Planet. Space Sci., 27, 881–884.
Ong, R. S. B., and N. Roderick, 1972. On the Kelvin Helmholtz instability of the Earth's magnetopause, Planet. Space Sci., 20, 1–10.
Patel, M. R., A. Bérces, C. Kolb, H. Lammer, P. Rettberg, J. C. Zarnecki, and F. Selsis, 2003. Seasonal and diurnal variations in Martian surface ultraviolet irradiation: biological and chemical implications for the Martian regolith, Int. J. Astrobiology, 2, 21–34.
Pérez–de–Tejada, H., 1998. Momentum transport in the solar wind erosion of the Mars ionosphere, J. Geophys. Res., 103, 31499–31508.
Petrinec, S. M., and C. T. Russell, 1997. Hydrodynamic and MHD equations across the bow shock and along the surfaces of planetary obstacles, Space Sci. Rev., 79, 757–791.
Russell, C. T., J. G. Luhmann, R. C. Elphic, F. L. Scarf, and L. H. Brace, 1982. Magnetic field and plasma wave observations in a plasma cloud at Venus, Geophys. Res. Lett., 9, 45–48.
Shinagawa, H., and T. E. Cravens, 1989. A one–dimensional multispecies magnetohydrodynamic model of the dayside ionosphere of Mars, J. Geophys. Res., 94, 6506–6516.
Shinagawa, H., and S. W. Bougher, 1999. A two–dimensional MHD model of the solar wind interaction with Mars, Earth Planets Space, 51, 55–60.
Tanaka, T., 1998. Effects of decreasing ionospheric pressure on the solar wind interaction with non–magnetized planets, Earth Planets Space, 50, 259–268.
Terada, N., S. Machida, and H. Shinagawa, 2002. Global hybrid simulation of the Kelvin–Helmholtz instability at the Venus ionopause, J. Geophys. Res., 107(A12), 1471–1490, doi:10.1029/2001JA009224.
Thomas, V. A., and D. Winske, 1991. Kinetic simulation of the Kelvin–Helmholtz instability at the Venus ionopause, Geophys. Res. Lett., 18, 1943–

1946.
Weitzner, H., 1983. Linear wave propagation in ideal magnetohydrodynamics, in Handbook of Plasma Physics, vol. 1, A. A. Galeev, and R. N. Sudan (eds.), North–Holland, New York, 201–242.
Wolff, R. S., B. E. Goldstein, and C. M. Yeates, 1980. The onset and development of Kelvin–Helmholtz instability at the Venusian ionopause, J. Geophys. Res., 85, 7697–7707.
Zwan, B. J., and R. A. Wolf, 1976. Depletion of the solar wind plasma near a planetary boundary, J. Geophys. Res., 81, 1636–1648.

Figure and Table captions:

Fig. 1: Instability growth rate for ideal MHD (dashed line), and including the finite Larmor radius effect and gravity (solid line), where the finite Larmor radius effect leads to the short–wavelength stabilization, while gravity gives the long–wavelength stabilization of the Kelvin–Helmholtz instability.

Fig. 2: Scheme of the principal configuration and terminology used in our model. The ionosphere has the normalized distance 1 from the center of Mars, the magnetosheath thickness is labeled Δ_s, and the bow shock distance from the center of the planet is x_s. IP refers to the ionopause, and BS to the bow shock.

Fig. 3: From top to bottom: the first panel is the mass density variations along different stream lines near the ionopause; the second panel is the total velocity variation along different stream lines; the last panel shows the stream lines along the ionopause, where the dashed line indicates the shape of the obstacle in the XZ–plane. The X-direction points from Mars to the Sun, Z is directed parallel to the IMF direction, and Y completes the right hand system.

Fig. 4a: Instability growth rate for an ionopause height of 400 km and a solar wind velocity of 400 km/s near the terminator.

Fig. 4b: Instability growth rate for an ionopause height of 1000 km and a solar wind velocity of 400 km/s near the terminator.

Fig. 5a: Instability growth rate for an ionopause height of 400 km and a solar wind velocity of 400 km/s at the flanks near the terminator plane.

Fig. 5b: Instability growth rate for an ionopause height of 1000 km and a solar wind velocity of 400 km/s at the flanks near the terminator plane.

Tab. 1: Loss of atomic oxygen from Mars by different escape processes.

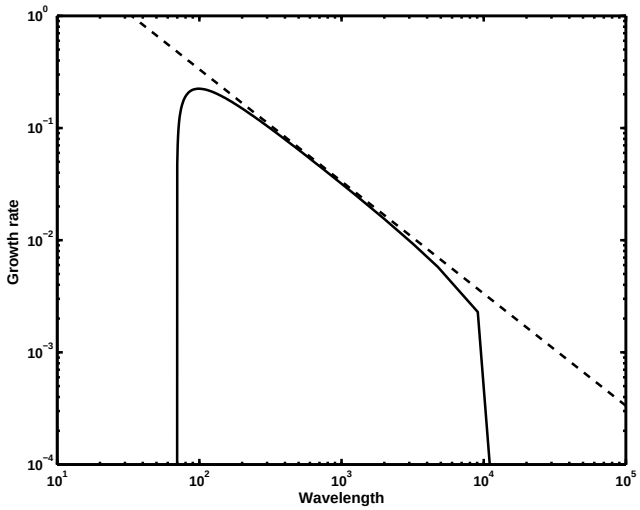
Growth rate
Wavelength
10^0
10^{-1}
10^{-2}
10^{-3}
10^{-4}
10^1
10^2
10^3
10^4
10^5

Fig. 1

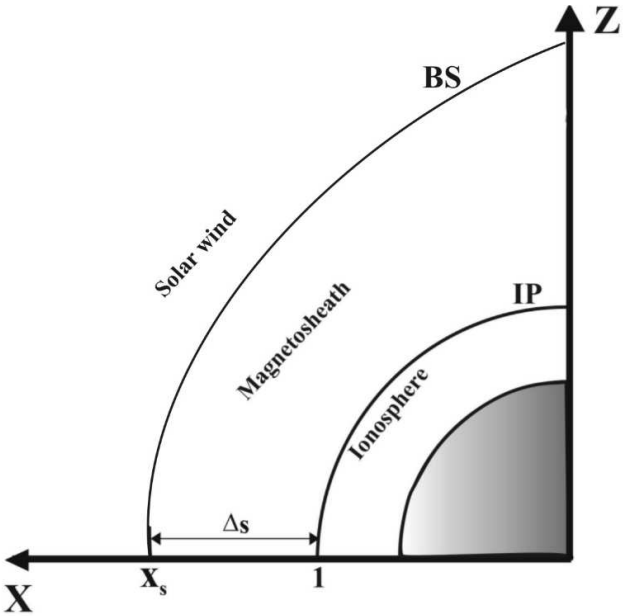

Fig. 2

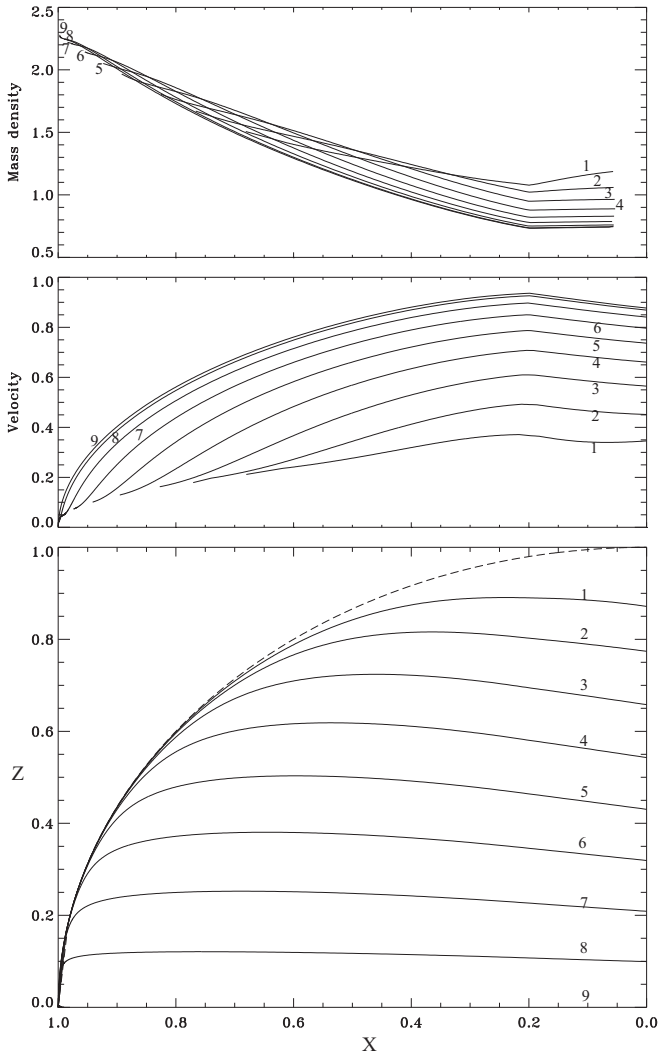

Fig. 3

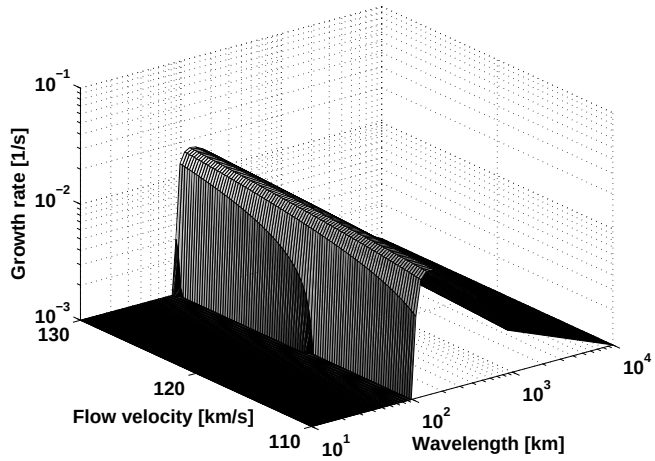
Growth rate [1/s]
10^−1
10^−2
10^−3
130
120
110
Flow velocity [km/s]
10^1
10^2
10^3
10^4
Wavelength [km]

Fig. 4a

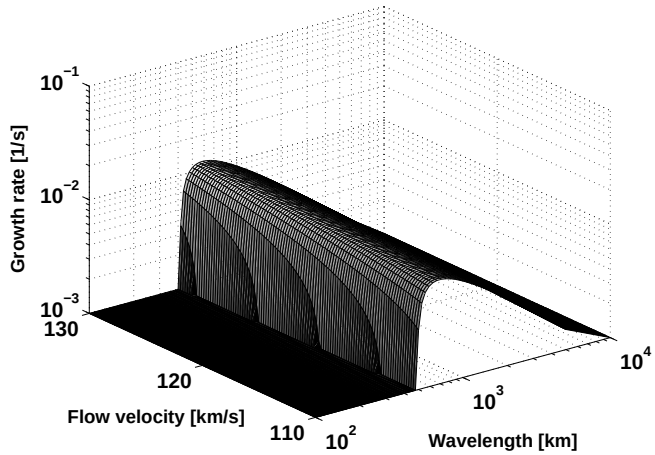
Growth rate [1/s]
10^−1
10^−2
10^−3
130
120
110
Flow velocity [km/s]
10^2
10^3
10^4
Wavelength [km]

Fig. 4b

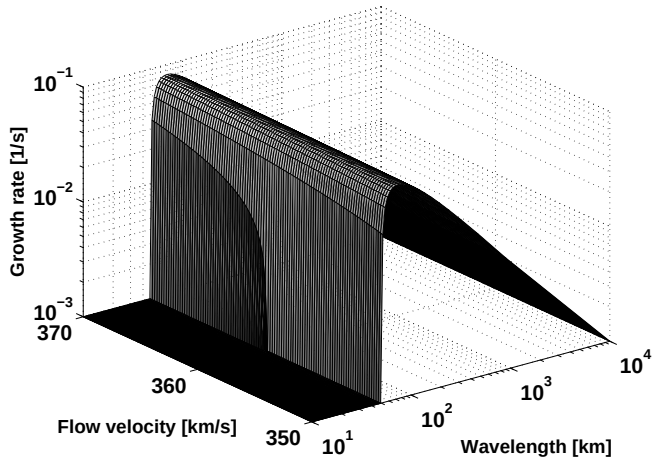
Growth rate [1/s]
10^−1
10^−2
10^−3
370
360
350
Flow velocity [km/s]
10^1
10^2
10^3
10^4
Wavelength [km]

Fig. 5a

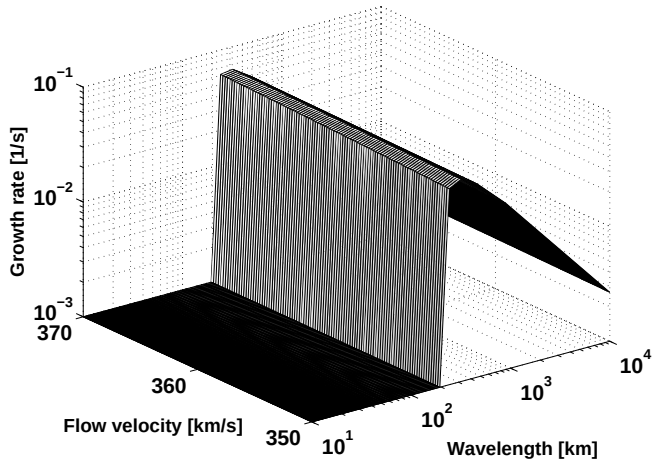
Growth rate [1/s]
10^−1
10^−2
10^−3
370
360
350
Flow velocity [km/s]
10^1
10^2
10^3
10^4
Wavelength [km]

Fig. 5b

Process	Loss of oxygen [s^{-1}]	Authors
Atmospheric sputtering	4.3 x 10^{23}	Leblanc and Johnson (2002)
Photochemical processes	5 x 10^{24}	Lammer and Bauer (1991)
Average ion pick up	3 x 10^{24}	Lammer et al. (2003a)
Plasma clouds maximum	3 x 10^{24}	this work
Plasma clouds minimum	2 x 10^{23}	this work

Tab. 1